Available online at www.sciencedirect.com

ScienceDirect

Tomography of Materials and Structures 00 (2024) 1–17

Journal Logo

www.elsevier.com/locate/procedia

Screening staining agents for contrast-enhanced microCT of vascular tissues: assessing the effect on microstructural and mechanical properties

M.Pétré[1,2,3], T. Balcaen[1,2,4], P. Schneidewind[2], L. Mazy[1,2,5], G. Pyka[1,2], H. Fehervary[3,6], N. Famaey[3,6] & G. Kerckhofs[1,2,5,7]

1. Institute of Mechanics, Materials and Civil Engineering (iMMC), UCLouvain, Belgium; 2. Institut de recherche expérimentale et clinique (IREC), UCLouvain, Belgium; 3. Dpt. Mechanical Engineering, KU Leuven, Belgium; 4. Chemistry Dpt., KU Leuven, Belgium; 5. Dpt. Materials Engineering, KU Leuven, Belgium; 6. FIBEr, KU Leuven Core Facility for Biomechanical Experimentation; 7. Prometheus, Division of Skeletal Tissue Engineering, KU Leuven, Belgium.

Abstract

Cardiovascular tissues possess a complex microstructure, which remodel and adapt due to ageing and diseases. This complex and evolving microstructure is intrinsically linked to the tissue's mechanical properties. To better understand how changes in the microstructure can impact the mechanical behavior, 4D-contrast-enhanced microCT (4D-CECT) can be used (i.e. in situ mechanical loading combined with 3D microstructural visualization). Since absorption-based CECT requires the use of contrast-enhancing staining agents (CESAs), we investigated six different CESAs for their suitability for 4D-CECT imaging of arterial tissue, considering their ability to provide good microstructural visualization and segmentation while ensuring the preservation of the mechanical properties. For this purpose, the penetration speed, contrast-enhancement, volume change, and stiffness change of porcine arterial tissue stained with the different CESA solutions were studied. Based on our results, we selected 1:2 Hafnium-substituted Wells-Dawson Polyoxometalate as the most suited CESA for 4D-CECT of arterial tissue. Phosphotungstic acid (PTA) and Lugol iodine with Sorensen's buffer (Lugol), despite being the reference in the state-of-the-art as CESA and having excellent contrast-enhancement properties, were the only ones that significantly affected the mechanical properties of porcine arterial tissue. Additionally, for these two solutions, tissue shrinkage was observed, resulting in a volume reduction of approximately −12% for PTA and −17% for Lugol. Finally, it was observed that the penetration speed of all CESA solutions exhibited a ratio of 60% to 40% from the intimal side to the adventitial side, which is likely due to the denser packing of elastic lamellae towards the adventitia. Overall, our study offers valuable new insights for selecting and comparing various CESA solutions for (4D-)CECT.

Keywords: 4D-contrast-enhanced microCT, mechanical characterization, arterial tissue, contrast-enhancing staining agent, biomechanics.

1. Introduction

Understanding how the microstructure of cardiovascular tissues influences the mechanical behavior can provide crucial insights into disease progression and can help to improve treatment planning, for diseases such as aneurysm formation, arterial dissection, or atherosclerosis. Thanks to microscopy techniques such

as second harmonic generation, fluorescence microscopy, and brightfield microscopy, the microstructure of vascular tissues can be visualized (i.e. collagen fibers, elastic lamellae, smooth muscle cells...) [1, 2, 3]. This microstructural information has already helped to create macroscopic, i.e. tissue-scale, constitutive models to predict the mechanical behavior of vascular tissues, such as the Gasser-Ogden-Holzapfel (GOH) model, where the collagen fiber orientation is taken into account [4]. Even though these macroscopic constitutive models already allow for a fairly accurate representation of the mechanical behavior of healthy vascular tissues, it is more difficult to define a constitutive model that represents the behavior of diseased vascular tissues. Tsamis *et al*. showed with classical 2D histology that, in the case of disease, vascular tissues often present high microstructural disorganization or damage both in terms of content and of architecture of the fibrous constituents (i.e. elastic lamellae and collagen fibers). These changes affect the mechanical behavior and strength associated with these conditions [5]. Nevertheless, accurately quantifying the disorganization or damage present in the full tissue of interest is challenging since classical histology only offers 2D information from a limited number of tissue slices and can induce artifacts due to tissue sectioning. New microscopy methods like light sheet microscopy have demonstrated the ability to visualize mouse carotid arteries in three dimensions and assess alterations like neointimal hyperplasia and arterial media volume changes [2]. Nonetheless, light sheet microscopy requires sample preparation involving tissue fixation and optical clearing, which can modify the tissue's mechanical properties. Indeed, hydrophobic, solvent-based clearing methods, often induce significant tissue shrinkage, likely due to tissue dehydration [6, 7]. However, novel optical clearing methods such as aqueous and hydrogel embedding tend to better preserve the tissue volume [8, 9]. Nevertheless, fixation, often performed with formaldehyde, can also lead to alteration in mechanical properties due to cross-linking [10].

MicroCT imaging has the potential to provide more insight compare to the previously mentioned techniques as it gives 3D microstructural information in a non-destructive way and does not require fixation or optical clearing. However, to visualize soft tissues with absorption-based microCT, a contrast-enhancing staining agent (CESA) needs to be added; this is referred to as contrast-enhanced microCT (CECT). These CESAs are chemical compounds containing X-ray opaque elements that show a different affinity for different tissue constituents, hence revealing the soft tissue microstructure [11, 12]. Still, CECT imaging alone is not sufficient to understand the link between the microstructural properties of vascular tissues and their mechanical behavior. Ideally, in-situ mechanical loading of the tissue and 3D visualization of the microstructural constituents is performed simultaneously. This new technique is referred to as 4D microCT, in which an in-situ testing stage is fitted within a microCT device, often a uniaxial tensile or compression stage. Several papers have already used 4D microCT to characterize mineralized tissue (i.e. bone and cartilage) of joints [13, 14] and to study fatigue behavior in polymers [15] and metals [16]. The same approach can be applied to soft tissue and is referred to as 4D-CECT. Helfenstein-Didier *et al.* were the first to our knowledge to use 4D-CECT to study arterial dissection [17]. They used a uniaxial tensile test stage and sodium polytungsate (SPT) as CESA. In their study, they explored only one CESA with two staining times (i.e. 24h and 48h) and showed that SPT did not influence the mechanical properties of their tissue. However, the presence of dark regions on the published CECT images revealed that these staining times were not sufficient to completely stain the tissue. Consequently, their data does not provide information on the mechanical behavior of fully stained tissue. Moreover, the elastic lamellae, essential load-bearing constituents of the arterial wall, were hard to distinguish on their images, making it impossible to track them for digital volume correlation purposes or to segment them for quantifying the microstructural changes during loading. Being able to accurately visualize the microstructure is essential for 4D-CECT to allow for an accurate calculation of the strains with digital volume correlation. Indeed, this technique relies on tracking features based on variations in grey values to accurately determine strain measurements [18].

The choice of the CESA to perform 4D-CECT is crucial, as it should enable the visualization of the microstructure of the tissue, without affecting the mechanical properties of the tissue of interest, as otherwise the true mechanical behavior would be lost (i.e. unaltered sample tested immediately after harvesting). In literature, phosphotungstic acid (PTA) is among the most used CESAs for soft tissue imaging [19, 20, 21]. Its popularity likely stems from its prior usage in classical 2D histology (e.g. Mallory's haematoxylin

[22, 23, 24] and in electron microscopy [25]. This molecule belongs to the class of polyoxometalates (POM) and has been used as a CESA in plenty of studies due to its high contrast-enhancement properties. However, it is known to affect tissue integrity, specifically causing tissue shrinkage, both in water and ethanol as a solvent [26, 27]. Moreover, ethanol on its own is also known as a dehydrating solvent. To avoid this shrinkage effect, de Bournonville *et al.*, explored several comparable POMs for soft biological tissue visualization using physiological buffered saline (PBS) solution as solvent [28]. They identified two POMs, Hafnium-Wells 1:2 Dawson POM (Hf-WD 1:2 POM) and Monolacunary-Wells Dawson POM (Mono-WD POM), that did not induce tissue shrinkage and enabled similar contrast-enhancing properties as PTA. Another frequently used CESA is the Lugol's iodine (Lugol) solution [29, 30, 31, 32]. Lugol solution has excellent contrast-enhancing properties for a wide range of soft tissues. Nonetheless, it also induces substantial tissue shrinkage. Indeed, Xia *et al.* showed that depending on the concentration of Lugol solution, rabbit and human tongues could shrink up to 30-50% [32]. To tackle this challenge, Dawood *et al.* showed that buffering the Lugol with a stronger buffer (i.e. Sorensen's buffer) reduced tissue shrinkage for mouse livers and fetuses [33]. Finally, many CESAs are used in the literature [12, 17, 34, 35, 36], but few studies quantify and compare the diffusion properties, the potential destructiveness, and their relative contrast enhancement. Often, no robust protocols are proposed and a trial-and-error methodology is applied.

In this context, the present paper aims at investigating different CESA solutions to identify the most-suited one for 4D-CECT of vascular tissues. Indeed, this CESA solution should provide: i) good contrast-enhancement properties, ii) allow accurate visualization and segmentation of the tissue constituents present in vascular tissues and iii) should not alter the mechanical properties of the tissue. For this purpose, this study first evaluated the contrast-enhancement properties and penetration speed of 6 different CESA solutions on porcine aorta samples using CECT imaging. Then, mechanical tests were performed to evaluate the potential change in stiffness induced by the staining process of different CESA solutions.

2. Materials and Methods

2.1. Tissue harvesting, sample preparation, and sample assignment.

Descending porcine aortas, obtained from the Westvlees slaughterhouse (Belgian Pork Group, Westrozebeke, Belgium), were cut into strips of 1cm by 1cm for low- and high-resolution CECT imaging, and in dogbone shape samples (i.e. 1cm width and 4cm long) along the circumferential direction for mechanical testing. A randomization process was applied so that every experimental group contained samples from different porcine aortas at different locations. Within 3 hours after harvesting, all samples were preserved at -80°C through a snap freezing step in -78°C isopentane [37]. No fixation was performed on the tissue.

For CECT imaging, 7 different experimental conditions were investigated. Six groups contained samples stained with different CESA solutions and one was a control physiological buffer solution (PBS) group. The PBS control group was used to determine the potential spontaneous deterioration of the tissue under the same conditions (i.e. time, room temperature). Triplicates were used for each condition for the CECT imaging part. For the mechanical tests, an additional experimental condition was added, the Post-Harvest control group. This group was mechanically tested immediately after thawing and is, therefore, considered the ground truth in terms of native mechanical properties.

Before imaging or mechanical testing, the samples were thawed at room temperature and were put into their respective CESA solutions at room temperature on a shaker plate to enhance the diffusion of the CESA through the tissue. An unstained sample refers to a sample being thawed and not immersed (yet) in the CESA solution (group 8) or immersed in a physiological buffer solution (group 7). A stained sample refers to a sample being placed in its CESA solution for a certain staining time (groups 1-6). Similarly, a fully stained sample refers to a sample where no penetration front of the CESA is seen anymore.

2.2. CESA solution.

Six different CESA solutions were prepared with 5 different CESAs. Two CESAs are synthesized in-house following literature procedures (Hf-WD 1:2 POM and Mono-WD POM [38, 39, 40]) and the three others are commercially available (PTA, SPT, and Lugol). The concentration of every CESA was selected based on the existing literature [17, 21, 28, 33] and can be found in Table 1. For PTA, an intermediate concentration of 2% was selected instead of 1% or 3% as found in the literature [19, 41]. Apart from the Lugol solution, all the other CESAs are in the form of a powder that can be dissolved in PBS. For a specific volume V, the CESAs were first dissolved in $V/2$ of physiological buffer 10 mM. Then, the pH was measured and adjusted to obtain a pH of 7.2 – 7.4 using HCL 6 M/ NaOH 5 M. Next, the remaining volume of miliQ water to reach the desired concentration ($V/2 - V_{HCl/NaOH}$) was added. Finally, the osmolality was measured for all solutions and corrected to obtain an osmolality of around 312 mOsm using NaCl (Table 1). Only for PTA, the pH was not corrected, as it is a strong acid (pH 2.18), and increasing the pH would modify the PTA present in the solution, leading to other POM species than PTA [42, 43]. Therefore, the samples were immersed in a PTA solution with a pH of 2.18. Lugol was buffered with Sorenson's buffer solution (i.e. for 80ml of total Lugol solution, 40ml phosphate buffer 266 mM at pH 7.16 were mixed with 20ml of Lugol and 20 ml of miliQ water [44]) and led to a hypertonic solution (545 $mOsm$ and pH 7.18). Every sample was placed in 5 ml of respective CESA solution or PBS solution for the PBS group, except for the Post-Harvest group. 5ml solution was on average about 30 times the sample volume (i.e. mean sample volume $153.4mm^3 \pm 34mm^3$).

Table 1: Contrast-enhancing staining agent solutions, their concentration, optimized pH and optimized osmolality.

CESAs	Concentration $[mg/mL]$	Molarity [mM]	Mass Percentage	Solvent	pH	Osmolality [mOsm]	Abbreviation
Hf-WD 1:2 POM [28]	35	3.69	3.5%	PBS	7.23	305	Hf
Lugol with Sorenson's buffer [33]	12.5 I_2	12.75 I_2, 39 KI	0.625% I_2, 1.25% KI*	Sorenson's buffer**	7.18	545	Lugol
Mono-WD POM [28]	35	7.12	3.5%	PBS	7.22	307	Mono 35
Mono-WD POM [28]	70	14.24	7%	PBS	7.19	297	Mono 70
PTA [21]	20	6.94	2%	PBS	2.18	305	PTA
SPT [17]	15	5.02	1.5%	PBS	7.48	307	SPT

*percentages after dilution, ** molarity of Sorenson's buffer equals 133 mM after dilution.

2.3. Contrast-enhanced microfocus computed tomography image acquisition.

Three samples per experimental group were placed in their respective solution for 3 hours, 6 hours, 9 hours, 1 day, 3 days, 5 days, 8 days, 15 days, and 17 days. At each time point, the samples were removed from their respective solution, slightly dried on a tissue, placed in a 3D-printed thin casing sample holder (i.e. in-house designed) to prevent motion and tissue dehydration, and imaged with the low-resolution protocol before being put back into their solution (Table 2). The low-resolution acquisition protocol enables to visualize the full volume of the sample and to track its volume change as well as the penetration speed of CESA solution. For the low-resolution imaging protocol, three samples were mounted vertically in a sample holder including two borosilicate beads to normalize the grey values in the reconstructed images. For the high-resolution imaging, only one sample per group was imaged at a time point of 17 days by selecting

and imaging a region of interest (ROI) of the sample, except for the SPT condition, for which three samples were imaged. The high-resolution acquisition protocol allows the discrimination of the different tissue constituents in the media of the aorta (i.e. elastic lamellae and ground matrix) and to assess the ease of segmentation of elastic lamellae after staining with the different CESA solutions. Figure 2 shows the workflow and the timeline used for the low and high-resolution imaging protocols. All samples were imaged using a Phoenix Nanotom M (GE Measurement and Control Solutions, Germany) equipped with a 180kV/15W energy nanofocus X-ray tube and a diamond-coated tungsten target. The acquisition and reconstruction parameters for both imaging resolutions are listed in Table 2. All CECT datasets were reconstructed with the Datos|x software (Backer Hughes Waygate Technologies, Germany) and exported as XY 16-bit slices (.tiff). For one sample of the PTA group at a time point 17 days, an in-house developed MATLAB (The MathWorks, Massachusetts, USA) script was used to convert the 16-bit slices (.tiff) to 8-bit slices (.bmp), while simultaneously normalizing the histogram range to the dynamic range of the dataset [45]. PTA 17 days was chosen as a reference as PTA gave the highest contrast enhancement. All the other datasets were normalized to that one using a second in-house developed MATLAB script with the borosilicate beads and the sample holder as reference materials [45].

Table 2: MicroCT acquisition and reconstruction parameters.

Parameters	Low-resolution protocol - All samples	High-resolution protocol - All samples
Voxel size (μm)	18	2.22
Source Voltage (kV)	120	92
Tube current (μA)	400	102
Mode	0	0
Number of images	1800	2400
Exposure time (ms)	500	750
Average	1	1
Skip	0	0
Fast scan mode	yes	no
Acquisition time (min)	15’	30’
Beam hardening correction	4	4
Inline median filter	yes	yes
ROI-CT filter	yes	yes
Filter Volume filter	yes	yes

2.4. Image analysis.

For the low-resolution datasets, the penetration of the CESA solutions inside the tissue was analyzed by measuring the penetration front depth at each time point. Per dataset, 10 slices evenly spaced out were analyzed, and every front depth was measured at two different locations on the slice (on n=3 samples per condition). This front can be seen in Figure 1, where the tissue grey values increase with the CESA diffusing in the tissue (i.e. grey values range from 0-255, where 0 is black and 255 is white). Both fronts in the media, starting from the adventitial and intimal side were measured. Then, the penetration front over the staining time was plotted in a log-log scale to obtain a linear fit for all the data points for every CESA using JMP Pro 16 (Statistical Discovery LLC, USA). Moreover, the initial penetration speed through the intima was computed based on the penetration front depth from the intimal side at a time point of 6 hours. Finally, the volume of every sample at each time point was computed in addition to the volume computed at the unstained state (time point 0 hours) using the Avizo software (Thermo Fisher Scientific, Bordeaux, France). The volume was assessed by segmenting the sample using manual segmentation and the interpolate function

in Avizo.

For the high-resolution datasets, first the contrast difference between the elastic lamellae and the extracellular matrix (i.e. also containing collagen fibers and smooth muscle cells, but cannot be distinguished from one another) was measured. For this, a large ROI was selected (Figure 1), where several profile lines of the same length perpendicular to the elastic lamellae were drawn with Dataviewer (Bruker microCT software, Germany) for several cross-sections. In total 50 measurements per dataset were made (n=1 sample per condition). Thanks to an in-house developed Python code, the peak and valley of every grey value profile line could be identified. The peaks are identified as the grey values corresponding to the elastic lamellae and the valley as the grey values corresponding to the ground matrix (i.e. containing smooth muscle cells, collagen fibers...). The mean and standard deviation of the grey values associated with these peaks and valleys were calculated to compute the contrast to noise ratio (CNR) as follows:

$$CNR = \frac{\mu_a - \mu_b}{\frac{1}{2}(\sigma_a + \sigma_b)} \tag{1}$$

where μ_a is the mean and σ_a the standard deviation of the elastin lamellae, and μ_b is the mean and σ_b the standard deviation of the ground matrix.

For the ease of segmentation of the elastic lamellae from the ground matrix, two smaller ROIs were selected in the media layer, one close to the intima and a second one close to the adventitia. The following filters were applied to each ROI with the same parameters using the Dragonfly software (Object Research Systems (ORS) Inc, Canada [46]): a) median filter with a kernel size 7, a cross shape, and 1 iteration b) unsharp filter with a kernel size 9, a standard deviation of 2 and unsharp factor of 1, c) Frangi 3D filter with a standard deviation of 2, gaussian kernel and binarization from 0.02. Additionally, on the raw ROI images, the number of elastic lamellae was computed as the sum of the number of peaks identified on the profile lines.

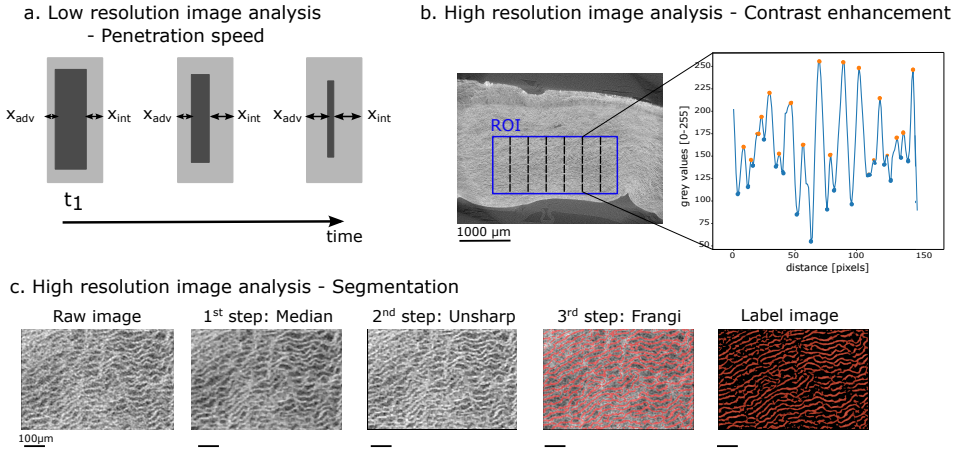

Fig. 1: Low and high-resolution image analysis protocol for the penetration speed (a), the contrast enhancement (b) and segmentation (c). The brighter grey region represents the region where the CESA solution has penetrated, and the darker grey region represents where it has not yet penetrated (a). x_{int} and x_{adv} front penetration depth on the intimal and adventitial side, respectively.

2.5. Uniaxial tensile tests and data processing.

As a uniaxial tensile test is destructive, different samples had to be used for the different time points. Therefore, four samples per experimental group and per time point were placed in their respective solution for 3 days, 8 days, and 17 days. The number of samples, which was four, was determined through a power analysis aimed at ensuring statistical significance. For the Post-Harvest group, 8 samples were tested immediately after thawing and for the PBS group 6 samples instead of four were tested at 3 days of immersion

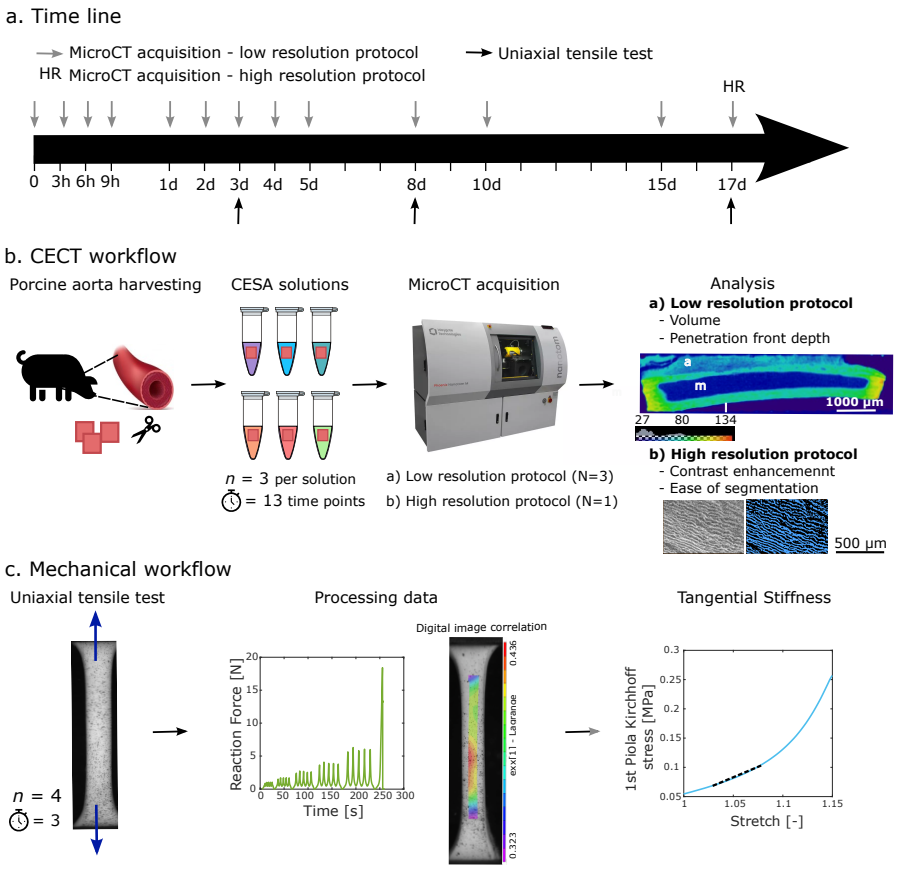

Fig. 2: Experimental workflow of the paper. (a = adventitia, m = media, i = intima and n = number of samples).

in the solution in addition to four samples for 8 and 17 days. Once immersed during their respective staining time, the sample thickness was measured with a micro-laser scanner (Gocator 2300, LMI technologies, Canada). Then, the samples were tested with a Messphysik-Zwick/Roell uniaxial tensile testing machine (Zwick/Roell, Germany) under displacement control. The samples were mounted using metallic toothed clamps and were placed in a PBS liquid bath at 37°C to replicate the in vivo conditions. A preload of 0.5 N was applied to avoid sagging of the sample and loads were applied with increasing magnitude at a set testing speed of 1 mm/s. Preconditioning of 5 loading cycles was repeated for every load magnitude step going from 5% load to 50% load with 5% load increments. A typical uniaxial test with these conditions lasts 5 minutes. A speckle pattern with graphite powder was deposited on the sample for strain mapping with 2D digital image correlation (DIC) using the software VIC-2D (Correlated Solutions, USA). The area of interest to compute the correlation was defined by the neck region of the dogbone sample in its reference configuration. A subset of 53 pixels and a step size of 7 pixels were used. Thanks to the VIC-2D DIC analysis, the spatial distribution of the Green-Langrange strain components along the principal experimental direction (i.e. circumferential direction) was computed. The 1^{st} Piola-Kirchhoff stress P was computed by dividing the reaction forces measured $RF(t)$ by the undeformed cross-sectional area A_0. The 1^{st} Piola-Kirchhoff stress-stretch curve was plotted and the tangential stiffness corresponding to the slope of the curve was computed at a stretch level of $\lambda = 1.1$. Figure 2 represents the workflow of the mechanical tests once the samples were stained, including the thickness measurement taken.

2.6. Statistical analysis.

JMP Pro 16 (Statistical Discovery LLC, USA) and GraphPad Prism 9 (GraphPad Software, USA) were used for the statistical analysis and data visualization. To compare the mechanical properties of the 6 stained groups with the Post-Harvest and PBS control groups, student's t-tests were performed after logarithmic transformation of the measured values to guarantee normality. The comparisons were made two by two between the Post-Harvest group and each of the stained groups as well as the PBS control group. Then, the Bonferroni correction was applied, which consists in multiplying the p-values obtained by a correction factor equal to the number of comparisons made minus one. To assess whether the staining time had an influence on the mechanical properties within the same staining group, a Tuckey test was performed for the three different staining time points within one stained group. Then, again the Bonferroni correction was applied to the obtained p-values. To compare the initial penetration speed and the volume difference from unstained to stained samples of the different CESAs solutions, an ordinary one-way ANOVA with Tukey's multiple comparisons test was performed. A p-value lower than 0.05 is considered significantly different and is denoted by $*$, $p < 0.01$ is denoted by $**$, and $p < 0.001$ is denoted by $***$ in the following Figures.

3. Results

All CESA solutions increased the contrast of the tissue constituents and revealed the elastic lamellae in porcine aortic tissue.

Elastin and collagen fibers are two fibrous constituents present in arteries that play an important role in the mechanical behavior. Being able to accurately visualize them is crucial to better understand the link between the microstructure and its mechanical behavior. Thanks to CECT, it is possible to accurately visualize in 3D the elastic lamellae present in arteries (Fig. 3). Here, we demonstrate the differences in contrast enhancement and the segmentation of elastic lamellae for all six CESA solutions. First, we quantified the contrast enhancement resulting from every CESA solution at low-resolution after 17 days of staining (18 μm voxel size - Fig. 3). PTA and Lugol staining gave the highest contrast increase (i.e. an absolute mean grey value of 193.7 ± 10.1 GV and 164.5 ± 6.5 GV, respectively), followed by Hf (119±0.5 GV). Doubling the concentration of Mono-WD POM slightly increased the contrast by about 10% (i.e. Mono 35: 93.7±1.5 GV, Mono 70: 102.7±0.6 GV). SPT (83.4 ± 2.6 GV) resulted in the smallest contrast increase. Unstained samples had a mean grey value of 39 ± 0.5 GV. A well-suited CESA solution should not only provide contrast increase globally but should also allow to distinguish the tissue constituents, such as the elastic lamellae from the ground matrix and to easily segment them. Therefore, the contrast to noise ratio (CNR) between the elastic lamellae (appearing bright grey) and the ground matrix (appearing darker grey) was analyzed for every CESA solution at high-resolution (2.2 μm voxel size). Moreover, two regions of interest (ROIs) were selected to characterize the ease of segmentation of the elastic lamellae; one ROI closer to the adventitia layer and a second ROI closer to the intima layer. Hf gave the highest contrast to noise ratio, followed by Lugol and PTA. Indeed, the elastic lamellae are highly distinguishable from the background for Hf, Lugol and PTA, enabling a smooth and easy segmentation. Mono 35, Mono 70, and SPT displayed lower contrast to noise ratio. Although at the low-resolution scale doubling the concentration of Mono-WD POM increased the contrast enhancement, at the high-resolution it decreased slightly the CNR. Indeed, when looking at the two ROIs of Mono 70, the elastic lamellae are difficult to distinguish, and therefore, the segmentation contained more noise characterized by speckles. SPT solution induced a fuzziness and blurriness of the elastic lamellae. The high-resolution image acquisition was repeated for three samples and the presence of fuzziness was consistently observed in each of them. Moreover, the SPT compound was reduced during the staining process, evidenced by samples obtaining a deep blue color [47, 48].

The penetration speed of the CESA solutions varies between CESAs and from the intimal side to the adventitial side.

As potential deterioration of the tissue could arise during the staining process performed at room temperature, it is important to know on average the minimal staining time needed for the different CESA solutions for full staining. Therefore, we investigated the penetration speed of the different CESA solutions. All

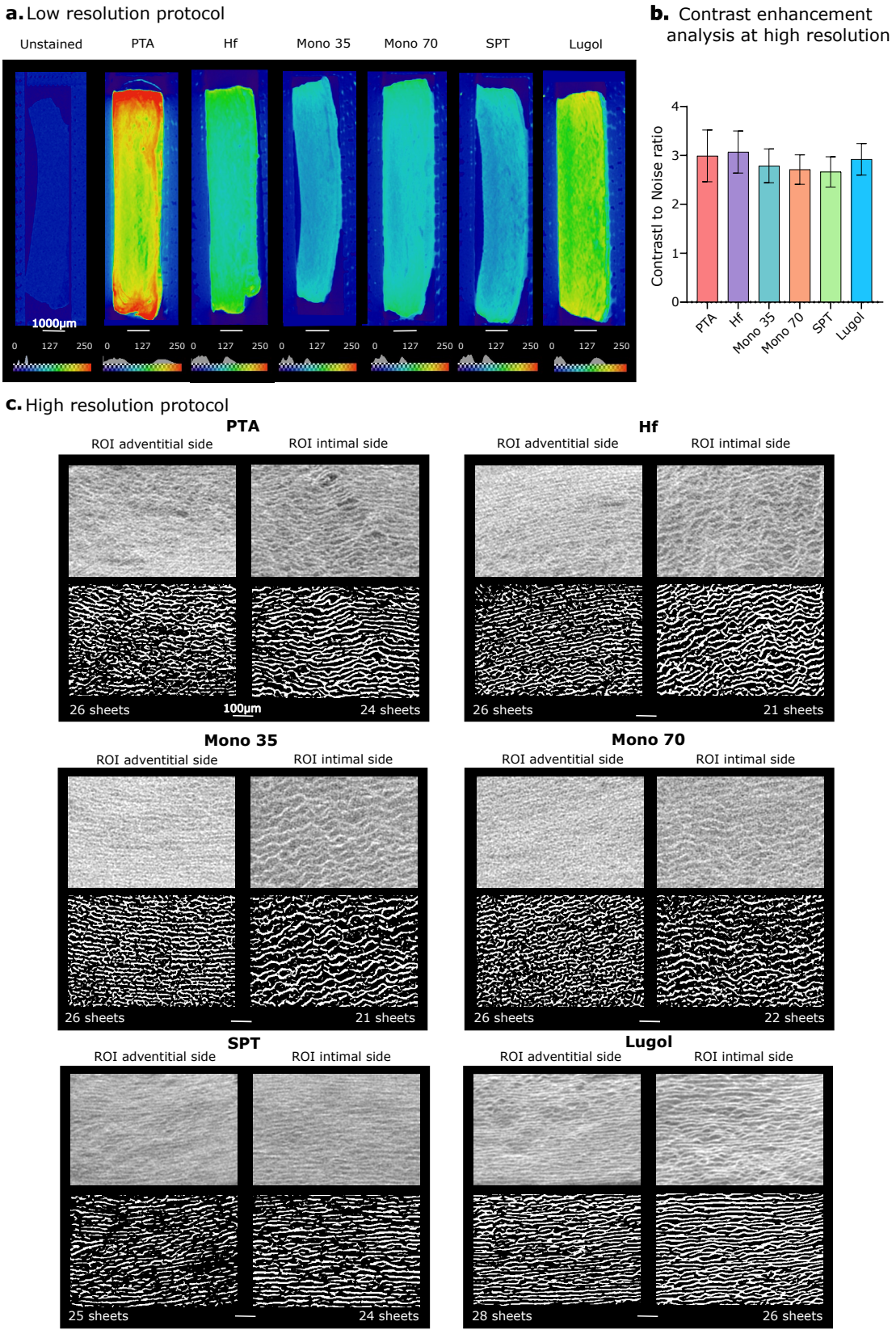

Fig. 3: Contrast-enhancement of the different CESA solutions for the low-resolution protocol, n=3 **(a)**. Contrast to noise ratio between the elastic lamellae and the ground matrix for the different CESA solutions **(b)**. Bars represent the mean, and error bars indicate the standard deviation for multiple measurement obtained on one sample (n=1). High-resolution protocol with a zoom on two regions of interest one close to the adventitia and a second one closer to the intima, where elastic lamellae were segmented for each CESA solutions and the number of elastic lamellae was computed, n=1 **(c)**.

CESAs exhibit slower diffusion within the tissue when coming from the adventitial side in comparison to the intimal side. On average, there is approximately 60% penetration of the CESA from the intimal side, whereas the adventitial side shows a penetration of around 40%. This 60%-40% ratio was independent of the adventitia thickness, which varied strongly from one sample to another (Figure 4). This means that the adventitia layer (i.e. its microstructural constituents and thickness) was not responsible for slowing down the penetration of the CESAs in the tissue. Moreover, the penetration speed varied from one CESA solution to another and was not constant over time (Fig. 4.a-b). Lugol solution is the fastest to penetrate the tissue (initial intimal penetration speed 3884 $\mu m/day$), followed by both Mono-WD POM solutions. Doubling the concentration of Mono-WD POM did not significantly increase the penetration speed (2642 $\mu m/day$ for Mono 35, 2811 $\mu m/day$ for Mono 70). SPT solution had an intermediate penetration speed of 1927 $\mu m/day$. Hf and PTA solutions possessed the lowest penetration speed with no significant differences between the two POM solutions (1084 $\mu m/day$ for Hf, 938 $\mu m/day$ for PTA). Knowing that the average thickness of the 18 different samples at their unstained state was 1631±279 μm, it shows that the penetration speed is non-linear and decreases over time. For example Mono-WD POM solution requires two to three days to reach full staining of the tissue, although its initial intimal speed is 1.5 times the average sample thickness.

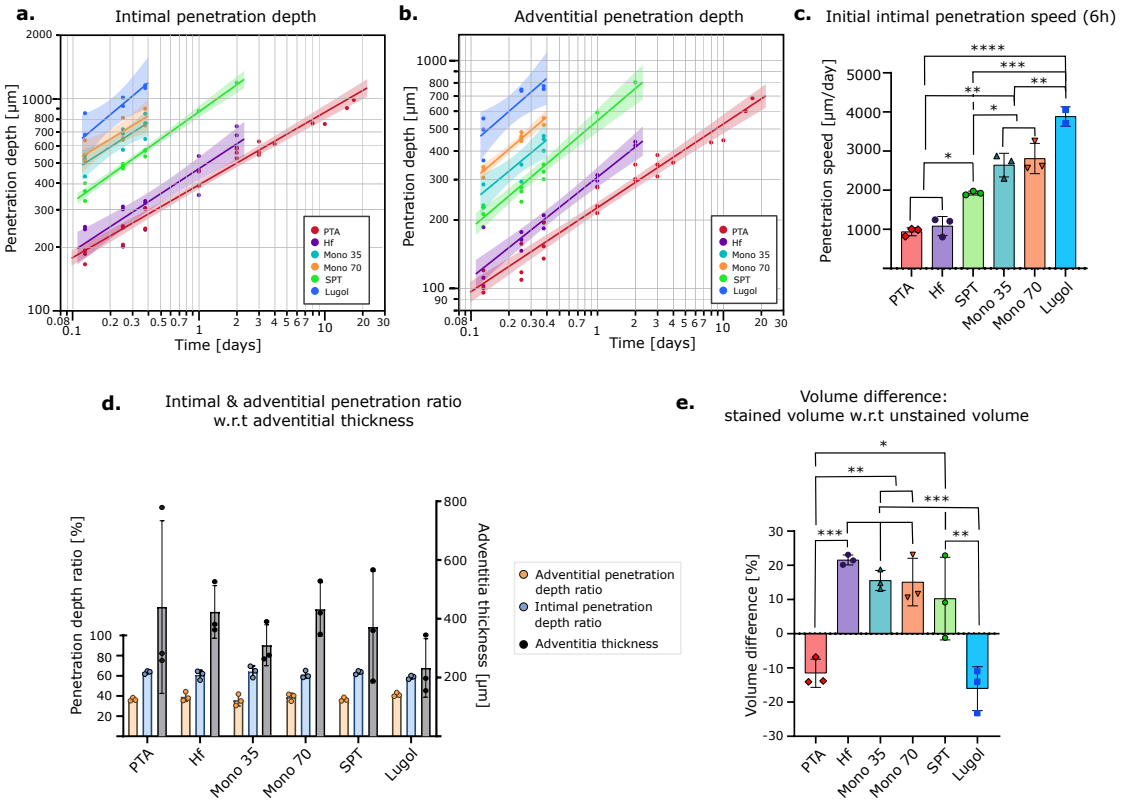

Fig. 4: Graphs representing the intimal (**a**) and adventitial (**b**) penetration depth in function of time in a log-log scale. The initial intimal penetration speed is computed at 6h and compared for the different CESA solutions (**c**). The intimal and adventitial penetration ratio is shown for every CESA solution with respect to their individual adventitial thickness (**d**). Swelling or shrinkage effect were measured for every stained sample with respect to their unstained volume (**e**). Bars represent the mean, and error bars indicate the standard deviation (n=3).

The staining process causes volume changes for the different CESA solutions.

Not only the contrast enhancement or penetration speed is important when selecting a suitable CESA for 4D-CECT, but also the potential destructiveness of the CESA solution. Here, we quantified the degree of relative

tissue shrinkage/swelling compared to their unstained volume. Despite Lugol solution being buffered with Sorensen's buffer, it caused an important initial tissue shrinkage (-10.5% after 3 hours and -15.5% after 6 hours), which continued to increase up to -17.1% after 1 day, at which all samples stained with Lugol were fully stained. PTA solution was the only POM solution that also caused a noteworthy tissue shrinkage at the end of the staining process (-12.1% after 17 days, at which all PTA samples were fully stained). All the other POM solutions caused swelling of the tissue. Hf solution induced the strongest swelling (+18.5% after 6 hours and +21.6% after 8 days of staining at which all Hf samples were fully stained). No significant difference in swelling was obtained for the two different concentrations of Mono-WD POM (+11.5% for Mono 35 and +11% for Mono 70 after 6 hours of staining, +15.6% for Mono 35 and +15.1% for Mono 70 after 3 days of staining at which all Mono 35 and Mono 70 samples were fully stained). SPT solution induced the least swelling (+5% after 6 hours and +9.8% after 3 days at which all SPT samples were fully stained) with, however, the highest variability (i.e. 95% lower and upper confidence intervals on the mean: -18.48 to 38.17).

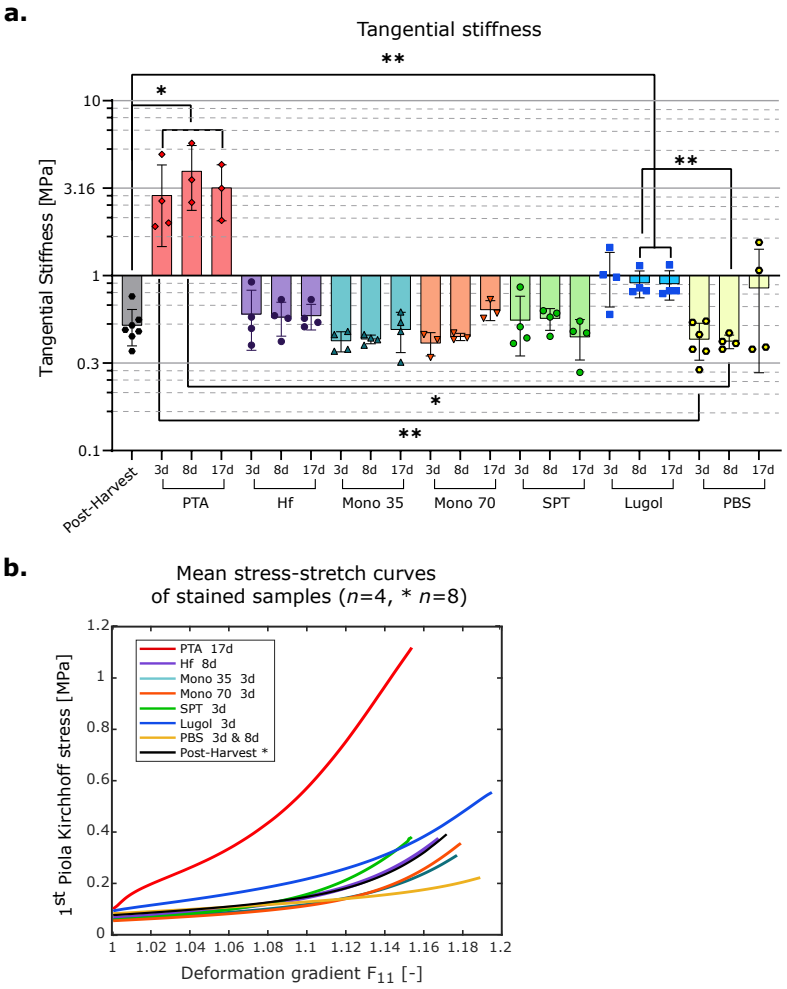

Fig. 5: The tangential stiffness is shown for the different CESA solutions at the different time points in a log scale (**a**). Bars represent the mean, and error bars indicate the standard deviation (n=4 for all CESA solutions, n=8 for Post-Harvest group and n=6 for PBS 3 days). The mean 1st Piola Kirchhoff stress-stretch curve of the stained samples (**b**).

PTA and Lugol solutions affect the mechanical properties of vascular tissues.

Being able to mechanically load arterial tissue and visualize the microstructural constituents deforming with 4D-CECT could help us to better understand disease progression and better predict when to perform an intervention. However, the CESA solution used for 4D-CECT should not influence the mechanical properties of the arterial tissue. We investigated the stiffness change induced by the six CESA solutions compared to the Post-Harvest group and the PBS group (Fig. 5). For all the conditions, the staining time did not show significant influence (Fig. 5.a). The in-house synthesized POMs and SPT solutions did not alter the mechanical properties. However, PTA did significantly alter the mechanical properties (+513% stiffness change for PTA 17d) in comparison with the Post-Harvest group. Lugol solution also induced a significant stiffness increase for the time point 8 days (+74%) and 17 days (+72%) with respect to the Post-Harvest group. Lugol and PTA solutions are, therefore, unsuitable for 4D-CECT.

4. Discussion

CECT imaging provides non-destructive 3D microstructural information on soft biological tissue. In literature, various compounds have been employed as contrast-enhancing staining agents (CESAs). However, limited understanding exists regarding their impact on microstructural and mechanical properties. Nevertheless, when aiming to integrate CECT imaging with in situ mechanical testing (4D-CECT), it is crucial to ensure that the selected CESA does not modify the mechanical properties of the tissue. Therefore, we investigated six different CESA solutions based on three imaging criteria (i.e. penetration speed, contrast enhancement, ease of segmentation) and two mechanical criteria (i.e. volume and stiffness change). For each criterium, we attributed a positive sign (+) or negative sign (−) to indicate the strengths and limitations of each CESA solution (Table 3). We demonstrated that the Hf solution is suitable for 4D-CECT of arterial tissue, and it is our preferred choice due to its ability to enhance contrast and to not affect the mechanical properties.

Table 3: Comparison of the different CESA solutions for their contrast-enhancement and influence on the mechanical properties (+ referred to a positive contribution, − referred to a negative contribution).

	Imaging Criteria			Mechanical Criteria	
CESA solutions	Penetration speed	Contrast Enhancement	Ease of Segmentation	Volume Change	Stiffness Change
PTA	-	+	+	-	-
Hf	-	+	+	-	+
Mono 35	+	-	-	+	+
Mono 70	+	-	-	+	+
SPT	+	-	-	+	+
Lugol	+	+	+	-	-

For all the CESA solutions investigated in this study, we have shown that the penetration speed differed from the intimal side to the adventitial side and followed a 60%-40% penetration ratio, respectively. This ratio is independent of the adventitia layer thickness, which varied strongly from one sample to another. We hypothesize that this 60%-40% ratio can be due to the denser packing of the elastic lamellae towards the adventitia (Fig. 4.d). Another hypothesis could be that the POMs and Lugol have a higher affinity with elastin lamellae, resulting in a slower diffusion process if the protein density increases towards the adventitia layer. Hence, when determining the average staining time required for a specific thickness of an elastic arterial tissue sample, it is essential to consider the difference in microstructure between the adventitial side and the intimal side.

In this study, we included PTA as it is a widely used CESA in the field of CECT. In the literature, PTA is mostly reported to be dissolved in ethanol or water but both caused substantial tissue shrinkage [20, 49]. Here, we investigated PTA (2 mg/ml) dissolved in PBS. It resulted in very good contrast enhancement and good contrast difference between the elastic lamellae and the ground matrix, facilitating the segmentation and shedding light on why this CESA is used so frequently despite its known tissue shrinkage effect. Indeed, PTA dissolved in PBS also induced significant tissue shrinkage (-12% after 17 days of staining) and significantly affected the mechanical properties of arterial tissue. This tissue shrinkage and stiffening of the tissue could be related to the high acidity, concentration or super-chaotropic behavior of PTA [50, 51]. The acidity of the PTA solution could induce coagulation of nucleic acids and certain proteins, leading to increased stiffness. The difference in PTA solution concentration compared to other CESA solutions makes it difficult to exclude a concentration effect, which could contribute to a stiffer mechanical behavior. Moreover, PTA and SPT in our study are chaotropic POMs, characterized by low charge density and high symmetry, unlike Hf and Mono, which have higher charge density. Buchecker et al. demonstrated that certain POMs with delocalized charges and sufficient size exhibit a super-chaotropic nature. Upon binding of a chaotropic ion to a protein, hydration water molecules are released from both the ion and the surface into the bulk water, resembling dehydration [50]. This could explain the significant shrinkage induced by PTA solution and the resulting stiffening of mechanical properties. However, despite also being chaotropic, SPT does not exhibit such behavior. Therefore, dedicated experiments are required to confirm these hypotheses, including a tissue integrity study and stiffness analysis based on incubation time, for different solutions with varying pH levels, containing chaotropic and less-chaotropic POMs at different concentrations and incubation times. However, based on our findings, we do not recommend using PTA for 4D-CECT imaging.

Lugol solution gave excellent contrast-enhancement of the elastic lamellae and allowed accurate segmentation of them. Despite the use of a buffered Lugol's solution as described by Dawood *et al.* [33] to limit volume shrinkage, this Lugol solution with Sorensen's buffer induced the most tissue shrinkage of all CESA solutions investigated. It also led to a high stiffness change, which was significantly different from the post-harvest group for a staining time above 8 days. 3 days of staining were sufficient to reach full staining of the arterial tissue and the stiffness change induced by Lugol solution was not significant for 3 days of staining. Still, we would not recommend this CESA for 4D-CECT, as despite the use of a stronger buffer and in contrast to Dawood *et al.* [33], high tissue shrinkage was present after only a few hours in the staining solution (-10.5% after 3 hours). The tissue shrinkage could be partially due to the hypertonicity of the solution (545 mOsm). However, Maes *et al.* used an isotonic Lugol (i.e. final molarity of 5mM) and also reported significant tissue shrinkage for bovine muscular tissue (-19% after 1 day of staining) [37].

SPT solution was included as potential CESA candidate for 4D-CECT because Helfenstein-Didier *et al.* used it to study arterial dissection under 4D-CECT [17]. In their study, they imaged samples stained for 1 day and 2 days at low-resolution. However, on their images, it was clear that SPT had not fully diffused in the tissue as dark regions, indicative of unstained tissue, were still present in their images. Our results showed that the minimal staining time for SPT solution was 3 days to reach full staining of porcine aortic tissue. They mentioned that they did not further increase the staining time because they observed a fuzziness in their images [17]. We imaged three samples stained 17 days with SPT at high-resolution (i.e. 2.22μm) and we confirm the presence of fuzziness (Fig. 3). In terms of contrast to noise ratio, SPT solution still gave a similar value to Mono-WD POM solutions and induced the least volume change of all CESA solutions (+9.8%) with, however, a large deviation on the mean (i.e. 95% lower and upper confidence intervals: -18.48 to 38.17). Helfenstein-Didier *et al.* mentioned that SPT had no effect on the mechanical properties compared to their control group, but only mechanically assessed it for one staining time point (1 day). We confirm that the SPT solution induced no change in mechanical properties for staining time points up to 17 days. The SPT solution is not the preferred choice for 4D-CECT due to the presence of fuzziness observed in the CECT images.

For the in-house synthesized POMs, the Hf solution possessed similar imaging results to Lugol and PTA solutions, with a high contrast difference between the elastic lamellae and the background as well as good

segmentation results. Mono 35 and Mono 70 solutions, on the other hand, gave lower contrast-enhancement, especially for Mono 70 for which the distinction of the elastic lamellae was more complicated and the segmentation of it was more noisy and speckled compared to the other CESA solutions. This could indicate unspecific deposits of the POM between the elastic lamellae. In contrast to the PTA solution, they all induced a swelling of the tissue. Hf solution induced the most swelling (+21.5%). However, the Hf samples were the first ones to be imaged after thawing (at time point 0 h), and they spent comparatively less time in PBS compared to the other samples for the same imaging time point. This could suggest that the Hf samples rehydrated promptly after the thawing process, leading to potentially smaller swelling. Indeed, Lisa *et al.* demonstrated that the porcine aorta exhibited on average a swelling of +4% when stained with the Hf solution after , as compared to its fresh state [52]. Maes *et al.* showed that bovine muscle tissue swelled by +7% after 7 days due to Hf staining [45]. Mono 35 and 70 solutions induced less swelling and we showed that doubling the concentration of Mono-WD POM did not influence the swelling effect (15.5% for Mono 35 and 15% for Mono 70). Despite this swelling of the in-house synthesized POMs, no significant change in the mechanical behavior was observed for all staining time points. The Hf solution is our preferred option for 4D-CECT of arterial tissue because of its excellent contrast-enhancing properties and its absence of influence on the mechanical properties of porcine aorta.

Our study has some limitations. The use of porcine aortic tissue makes our findings only valid for elastic arterial tissue. This study could be extended to other types of blood vessels from different species, as well as other types of soft tissue to draw general conclusions about the suitability of a CESA for 4D-CECT. Moreover, all samples were snap-frozen at -78°C in liquid isopentane for preservation purposes before being thawed and mechanically tested. The effect of freezing on the mechanical properties has not been addressed in this study but would be interesting to explore in future research to better understand its potential influence on the material's behavior. Furthermore, the CESA solutions investigated in this study did not possess the same molar concentration. For each CESA, we selected typical mass percentages, based on literature, for which good contrast enhancement was reported. This makes the comparison between the different CESA solutions more complicated, as not only the CESA plays a role, but also its concentration in the solvent. Furthermore, the number of samples was limited. For the penetration speed and volume analysis, three samples per CESA solution were investigated, and only one sample per CESA solution was analyzed at higher resolution for contrast enhancement. For the influence on the mechanical properties, on average four samples per CESA solution per staining time point were used. Finally, the optimal staining time for each CESA solution could not be assessed, as it would require more samples and more staining time points. In this study, we gave an approximation of the staining time needed for every CESA solution, which is only valid for porcine aortic tissue. If other tissue types would be of interest, a new study should be conducted to estimate the optimal staining time required for this tissue.

5. Conclusion

Understanding the link between microstructural and mechanical properties of arterial tissue is crucial for better understanding how arteries adapts and remodels due to ageing and diseases. For this purpose, in situ mechanical loading combined with 3D microstructural imaging using CECT can be used and is referred to as 4D-CECT. In this study, we investigated six different CESA solutions for their suitability for 4D-CECT imaging of arterial tissue microstructure. We focused on three imaging criteria (penetration speed, contrast-enhancement, and ease of segmentation) and two mechanical criteria (change in volume and stiffness change) to evaluate and compare each CESA solution. PTA and Lugol were discarded for 4D-CECT due to their significant tissue shrinkage and stiffening effects, despite their excellent contrast-enhancement properties. Consequently, the remaining POMs exhibited the most favorable behavior by not affecting the mechanical properties. In terms of contrast enhancement and ease of segmentation, Hf displayed superior performance, rendering it the preferred CESA for 4D-CECT of arterial tissue. We also showed that the penetration speed of all CESA solutions followed a 60%-40% ratio from the intimal side to the adventitial side, possibly because of the denser packing of elastic lamellae towards the adventitia. Our study provides a

methodical strategy for selecting and comparing various CESA solutions for (4D-)CECT, offering valuable new insights.

Acknowledgments

This research benefited from the help of Catherine Rasse, statistical consultant of the Service de Méthodologie Statistique et de Calcul, technological platform of the UCLouvain - SMCS/LIDAM, UCLouvain. We would like to thank Walid El Aazmani for helping prepare the CESA solutions. M.P. acknowledges the Flanders Community of Belgium in the framework of a FWO project grant (G088020N) and a FWO-SB mandate grant (1S64923N). T.B. acknowledges the French Community of Belgium in the framework of a FRIA grant (40004158). T.B. and M.P. acknowledge the support from a FWO project (FWO; grant G088218N). L. Mazy acknowledges the Flanders Community of Belgium in the framework of a FWO-SB mandate grant (1S61623N). P.S. and G.K. acknowledge the Action de Recherche Concertée (ARC 19/24-097) - Fédération Wallonie-Bruxelles. G.P. acknowledges the support from the SBO project of the Research Foundation Flanders (FWO; grant S007219N). N.F. and H.F. acknowledge KU Leuven's Bijzonder Onderzoeksfonds for supporting the Core Facility FIBEr where the mechanical tests were performed (3E210166 KERNFAC FIBER). The X-ray microCT images were generated at the KU Leuven XCT Core Facility (supported by Jeroen Soete, research expert) and in the microCT lab of UCLouvain (Woluwe, IREC). Avizo 2022.1 (ThermoFisher Scientific, France) software acquisition was supported by the Fonds de la Recherche Scientifique – (FNRS - EQP - Tomo4D-U.N069.20)

References

[1] T. Boulesteix, A.-M. Pena, N. Pagès, G. Godeau, M.-P. Sauviat, E. Beaurepaire, M.-C. Schanne-Klein, Micrometer scale ex vivo multiphoton imaging of unstained arterial wall structure, Cytometry Part A: the journal of the International Society for Analytical Cytology 69 (1) (2006) 20–26.

[2] N. E. Buglak, J. Lucitti, P. Ariel, S. Maiocchi, F. J. Miller Jr, E. S. Bahnson, Light sheet fluorescence microscopy as a new method for unbiased three-dimensional analysis of vascular injury, Cardiovascular research 117 (2) (2021) 520–532.

[3] M. Ramella, P. Bernardi, L. Fusaro, M. Manfredi, F. Casella, C. M. Porta, L. Nicolai, E. Galeazzi, R. Boldorini, A. M. Settembrini, et al., Relevance of inflammation and matrix remodeling in abdominal aortic aneurysm (aaa) and popliteal artery aneurysm (paa) progression, American journal of translational research 10 (10) (2018) 3265.

[4] T. C. Gasser, R. W. Ogden, G. A. Holzapfel, Hyperelastic modelling of arterial layers with distributed collagen fibre orientations, Journal of the royal society interface 3 (6) (2006) 15–35.

[5] A. Tsamis, J. T. Krawiec, D. A. Vorp, Elastin and collagen fibre microstructure of the human aorta in ageing and disease: a review, Journal of the Royal Society Interface 10 (83) (2013) 20121004.

[6] W. D. Meador, J. Zhou, M. Malinowski, T. Jazwiec, S. Calve, T. A. Timek, M. K. Rausch, The effects of a simple optical clearing protocol on the mechanics of collagenous soft tissue, Journal of biomechanics 122 (2021) 110413.

[7] H. Dodt, U. Leischner, A. Schierloh, N. Jahrling, C. Mauch, K. Deininger, J. Deussing, M. Eder, W. Zieglgansberger, K. Becker, Ultramicroscopy: three-dimensional visualization of neuronal networks in the whole mouse brain., Nature methods 4 (2007) 331–336.

[8] T. I. Meng-Tsen Ke, Satoshi Fujimoto, Seedb: a simple and morphology-preserving optical clearing agent for neuronal circuit reconstruction, Nature Neurosciences 16 (2013) 1154–1161.

[9] Y.-G. Park, C. Ho Sohn, R. Chen, et al., Protection of tissue physicochemical properties using polyfunctional crosslinkers., Nature Biotechnology 37 (2019) 73–83.

[10] J. Braun, H. Tzschätzsch, C. Körting, A. Ariza de Schellenberger, M. Jenderka, T. Drießle, M. Ledwig, I. Sack, A compact 0.5 t mr elastography device and its application for studying viscoelasticity changes in biological tissues during progressive formalin fixation, Magnetic Resonance in Medicine 79 (2018) 470–478.

[11] S. de Bournonville, S. Vangrunderbeeck, G. Kerckhofs, Contrast-enhanced microct for virtual 3d anatomical pathology of biological tissues: a literature review, Contrast media & molecular imaging 2019.

[12] L. Leyssens, C. Pestiaux, G. Kerckhofs, A review of ex vivo x-ray microfocus computed tomography-based characterization of the cardiovascular system, International Journal of Molecular Sciences 22 (6) (2021) 3263.

[13] K. Madi, K. A. Staines, B. K. Bay, B. Javaheri, H. Geng, A. J. Bodey, S. Cartmell, A. A. Pitsillides, P. D. Lee, In situ characterization of nanoscale strains in loaded whole joints via synchrotron x-ray tomography, Nature biomedical engineering 4 (3) (2020) 343–354.

[14] P. J. Thurner, P. Wyss, R. Voide, M. Stauber, M. Stampanoni, U. Sennhauser, R. Müller, Time-lapsed investigation of three-dimensional failure and damage accumulation in trabecular bone using synchrotron light, Bone 39 (2) (2006) 289–299.

[15] S. S. Singh, N. Chawla, 3d/4d x-ray microtomography: probing the mechanical behavior of materials, in: Handbook of Mechanics of Materials, Springer Singapore, 2019, pp. 2013–2033.

[16] C. Jailin, A. Bouterf, M. Poncelet, S. Roux, In situ μ ct-scan mechanical tests: fast 4d mechanical identification, Experimental Mechanics 57 (2017) 1327–1340.

[17] C. Helfenstein-Didier, D. Taïnoff, J. Viville, J. Adrien, É. Maire, P. Badel, Tensile rupture of medial arterial tissue studied by x-ray micro-tomography on stained samples, Journal of the mechanical behavior of biomedical materials 78 (2018) 362–368.

[18] E. Dall'Ara, M. Peña-Fernández, M. Palanca, M. Giorgi, L. Cristofolini, G. Tozzi, Precision of digital volume correlation approaches for strain analysis in bone imaged with micro-computed tomography at different dimensional levels, Frontiers in Materials 4 (2017) 31.

[19] A. Hanly, R. D. Johnston, C. Lemass, A. Jose, B. Tornifoglio, C. Lally, Phosphotungstic acid (pta) preferentially binds to collagen-rich regions of porcine carotid arteries and human atherosclerotic plaques using 3d micro-computed tomography (ce-μct), bioRxiv, 2022, Cold Spring Harbor Laboratory.

[20] K. M. Lesciotto, S. M. Motch Perrine, M. Kawasaki, T. Stecko, T. M. Ryan, K. Kawasaki, J. T. Richtsmeier, Phosphotungstic acid-enhanced microct: Optimized protocols for embryonic and early postnatal mice, Developmental Dynamics 249 (4) (2020) 573–585.

[21] B. D. Metscher, Microct for comparative morphology: simple staining methods allow high-contrast 3d imaging of diverse non-mineralized animal tissues, BMC physiology 9 (1) (2009) 1–14.

[22] H. Puchtler, F. Waldrop, S. Meloan, On the mechanism of mallory's phosphotungstic acid-haematoxylin stain, Journal of Microscopy 119 (3) (1980) 383–390.

[23] M. M. Everett, W. A. Miller, The role of phosphotungstic and phosphomolybdic acids in connective tissue staining i. histochemical studies, The Histochemical Journal 6 (1974) 25–34.

[24] J. Y. TERNER, Phosphotungstic acid-hematoxylin. reactivity in vitro, Journal of Histochemistry & Cytochemistry 14 (4) (1966) 345–351.

[25] L. Silverman, D. Glick, The reactivity and staining of tissue proteins with phosphotungstic acid, The Journal of cell biology 40 (3) (1969) 761–767.

[26] R. Balint, T. Lowe, T. Shearer, Optimal contrast agent staining of ligaments and tendons for x-ray computed tomography, PloS one 11 (4) (2016) e0153552.

[27] M. Dunster-Jones, M. Steicke, J. Mackie, R. Guthrie, T. N. Dinh, F. Ahmady, J. Golledge, Y. Wang, The concentration of ethanol affects its penetration rate in bovine cardiac and hepatic tissues, Folia Histochemica et Cytobiologica 56 (2) (2018) 92–97.

[28] S. de Bournonville, S. Vangrunderbeeck, H. G. T. Ly, C. Geeroms, W. M. De Borggraeve, T. N. Parac-Vogt, G. Kerckhofs, Exploring polyoxometalates as non-destructive staining agents for contrast-enhanced microfocus computed tomography of biological tissues, Acta Biomaterialia 105 (2020) 253–262.

[29] P. M. Gignac, N. J. Kley, J. A. Clarke, M. W. Colbert, A. C. Morhardt, D. Cerio, I. N. Cost, P. G. Cox, J. D. Daza, C. M. Early, et al., Diffusible iodine-based contrast-enhanced computed tomography (dicect): an emerging tool for rapid, high-resolution, 3-d imaging of metazoan soft tissues, Journal of anatomy 228 (6) (2016) 889–909.

[30] P. Heimel, N. V. Swiadek, P. Slezak, M. Kerbl, C. Schneider, S. Nürnberger, H. Redl, A. H. Teuschl, D. Hercher, Iodine-enhanced micro-ct imaging of soft tissue on the example of peripheral nerve regeneration, Contrast Media & Molecular Imaging 2019.

[31] S. T. Robinson, R. E. Levey, R. Beatty, D. Connolly, E. B. Dolan, N. H. Osborne, P. Dockery, P. K. Henke, G. P. Duffy, A versatile technique for high-resolution three-dimensional imaging of human arterial segments using microcomputed tomography, JVS: Vascular Science 2 (2021) 13–19.

[32] C.-W. Xia, R.-l. Gan, J.-r. Pan, S.-q. Hu, Q.-z. Zhou, S. Chen, L. Zhang, Q.-G. Hu, Y.-X. Wang, Lugol's iodine-enhanced micro-ct: A potential 3-d imaging method for detecting tongue squamous cell carcinoma specimens in surgery, Frontiers in oncology 10 (2020) 550171.

[33] Y. Dawood, J. Hagoort, B. Siadari, J. Ruijter, Q. Gunst, N. Lobe, G. Strijkers, B. de Bakker, M. van den Hoff, Reducing soft-tissue shrinkage artefacts caused by staining with lugol's solution, Scientific reports 11 (1) (2021) 1–12.

[34] E. Descamps, A. Sochacka, B. De Kegel, D. Van Loo, L. Van Hoorebeke, D. Adriaens, Soft tissue discrimination with contrast agents using micro-ct scanning, Belgian Journal of Zoology 144 (1).

[35] J. M. d. S. e. Silva, I. Zanette, P. B. Noël, M. B. Cardoso, M. A. Kimm, F. Pfeiffer, Three-dimensional non-destructive soft-tissue visualization with x-ray staining micro-tomography, Scientific reports 5 (1) (2015) 14088.

[36] E. L. Scheller, N. Troiano, J. N. VanHoutan, M. A. Bouxsein, J. A. Fretz, Y. Xi, T. Nelson, G. Katz, R. Berry, C. D. Church, et al., Use of osmium tetroxide staining with microcomputerized tomography to visualize and quantify bone marrow adipose tissue in vivo, in: Methods in enzymology, Vol. 537, Elsevier, 2014, pp. 123–139.

[37] A. Maes, C. Pestiaux, A. Marino, T. Balcaen, L. Leyssens, S. Vangrunderbeeck, G. Pyka, W. M. De Borggraeve, L. Bertrand, C. Beauloye, et al., Cryogenic contrast-enhanced microct enables nondestructive 3d quantitative histopathology of soft biological tissues, Nature Communications 13 (1) (2022) 1–14.

[38] C. N. Kato, A. Shinohara, K. Hayashi, K. Nomiya, Syntheses and x-ray crystal structures of zirconium (iv) and hafnium (iv) complexes containing monovacant wells- dawson and keggin polyoxotungstates, Inorganic chemistry 45 (20) (2006) 8108–8119.

[39] A. P. Ginsberg, Inorganic Syntheses, Volume 27, Vol. 27, John Wiley & Sons, 1991.

[40] W. W. Laxson, S. Ozkar, R. G. Finke, Triniobium, wells–dawson-type polyoxoanion,[(n-c4h9) 4n] 9p2w15nb3o62: Improvements in the synthesis, its reliability, the purity of the product, and the detailed synthetic procedure, Inorganic Chemistry 53 (5) (2014) 2666–2676.

[41] D. De Greef, J. A. Buytaert, J. R. Aerts, L. Van Hoorebeke, M. Dierick, J. Dirckx, Details of human middle ear morphology based on micro-ct imaging of phosphotungstic acid stained samples, Journal of morphology 276 (9) (2015) 1025–1046.

[42] G. Quintarelli, M. Bellocci, R. Geremia, On phosphotungstic acid staining iv. selectivity of the staining reaction, Journal of Histochemistry & Cytochemistry 21 (2) (1973) 155–160.

[43] B. J. Smith, V. A. Patrick, Quantitative determination of aqueous dodecatungstophosphoric acid speciation by nmr spectroscopy, Australian journal of chemistry 57 (3) (2004) 261–268.

[44] Y. Dawood, J. Hagoort, B. Siadari, J. Ruijter, Q. Gunst, N. Lobe, G. Strijkers, B. de Bakker, M. van den Hoff, Author correction: Reducing soft-tissue shrinkage artefacts caused by staining with lugol's solution, Scientific Reports 12 (1) (2022) 1–1.
[45] A. Maes, Relative normalization of microCT datasets for grey value comparison (Mar. 2023). doi:10.5281/zenodo.7688929. URL https://doi.org/10.5281/zenodo.7688929
[46] Dragonfly 2023 [Computer software]. Object Research Systems (ORS) Inc, Montreal, Canada, 2020; software available at. URL http://www.theobjects.com/dragonfly
[47] J.-J. Chen, L. Vila-Nadal, A. Solé-Daura, G. Chisholm, T. Minato, C. Busche, T. Zhao, B. Kandasamy, A. Y. Ganin, R. M. Smith, et al., Effective storage of electrons in water by the formation of highly reduced polyoxometalate clusters, Journal of the American Chemical Society 144 (20) (2022) 8951–8960.
[48] M. Stojanović, J. Lalatović, A. Milosavljević, N. Savić, C. Simms, B. Radosavljević, M. Ćetković, T. Kravić-Stevović, D. Mrda, M. B. Čolović, et al., In vivo toxicity evaluation of a polyoxotungstate nanocluster as a promising contrast agent for computed tomography, Preprint, 2023.
[49] J. Buytaert, J. Goyens, D. De Greef, P. Aerts, J. Dirckx, Volume shrinkage of bone, brain and muscle tissue in sample preparation for micro-ct and light sheet fluorescence microscopy (lsfm), Microscopy and microanalysis 20 (4) (2014) 1208–1217.
[50] T. Buchecker, P. Schmid, S. Renaudineau, O. Diat, A. Proust, A. Pfitzner, P. Bauduin, Polyoxometalates in the hofmeister series, Chemical communications 54 (15) (2018) 1833–1836.
[51] S.-D. Albert, J. M. Poblet, J. J. Carbo, Structure-activity relationships for the affinity of chaotropic polyoxometalate anions towards proteins., Molecular Dynamics 26 (2020) 5799–5809.
[52] L. Leyssens, T. Balcaen, M. Pétré, N. B. Ayllón, W. El Aazmani, A. de Pierpont, G. Pyka, V. Lacroix, G. Kerckhofs, Non-destructive 3d characterization of the blood vessel wall microstructure in different species and blood vessel types using contrast-enhanced microct and comparison with synthetic vascular grafts, Acta Biomaterialia.